PAPER

Robust Surface Reconstruction in SEM Using Two BSE Detectors

Deshan CHEN[†a)], *Nonmember*, Atsushi MIYAMOTO[††b)], *and* Shun'ichi KANEKO[†c)], *Members*

SUMMARY This paper describes a robust three-dimensional (3D) surface reconstruction method that can automatically eliminate shadowing errors. For modeling shadowing effect, a new shadowing compensation model based on the angle distribution of backscattered electrons is introduced. Further, it is modified with respect to some practical factors. Moreover, the proposed iterative shadowing compensation method, which performs commutatively between the compensation of image intensities and the modification of the corresponding 3D surface, can effectively provide both an accurate 3D surface and compensated shadowless images after convergence.

key words: *scanning electron microscope (SEM), surface reconstruction, shadowing compensation, backscattering electron*

1. Introduction

The scanning electron microscope (SEM) is a very important tool for observing micro-structure and has been widely used in the areas of medical observation, semiconductors, material analysis, etc. The need for three-dimensional (3D) surface measurements is significantly increasing. For instance, 3D surface information can provide valuable clues for inspecting and analyzing defects in products of semiconductor manufacturing processes, such as recognition of device patterns and defect regions, classification of defects in terms of the processes responsible for their generation (surface/embedded defects [1]) and the impact on electric properties (volume or shorting/disconnection defect), and specification and control of the issue process, etc.

Attempts have been made to transform SEM into a 3D measuring tool for almost 30 years, and scientific research on 3D surface reconstruction in SEM continues to be intensively studied. Different approaches, which can be broadly classified into two groups, have been utilized. One popular group is generally referred to as the "stereometric" method [2]–[4], in which a pair of stereo images of a specimen at different inclination angles are taken, and the height or depth is determined by measuring the deviations of corresponding points on the two images. However, this method can only be applied to the measurements of surface points where recognizable fine structures exist. In general, it cannot be used on smooth surfaces or to reconstruct a continuous surface profile at high magnification.

The second group of approaches is the so-called "shape from shading" or "photometric stereo" method [5]–[10], in which multiple secondary or backscattered electron detectors (generally two or four) are symmetrically positioned about the beam axis, so that the gradient information on the surface being observed can be estimated from multiple images that are measured simultaneously by various detectors. The 3D surface is consequently obtained from the gradient information by an integration scheme. However, these studies have focused almost exclusively on deriving accurate gradient measurement formulas, i.e., expressions of the relationships between the gradient component(s) of target objects and the measured SEM signals from multiple detectors at the points of observation, in which shape information from the surrounding area is excluded. Signal values are generally influenced by shadowing effects associated with the surrounding topography, because such effects absorb a portion of the electrons and are the main source of errors in 3D measurements.

Paluszyński and Slówko [11] introduced several techniques for reconstructing the shape in the shadowed region that utilize two or three unshadowed detectors under a setting of four secondary electron (SE) detectors. However, this method requires exact geometric parameters for the detector system, which are generally difficult to obtain. In addition, shadowed regions must be manually identified from the SE images each time, which is restrictive for some actual applications.

The objective of this study was to robustly and automatically reconstruct an accurate 3D surface from SEM images in the presence of shadowing effects in SEM using two backscattered electron (BSE) detectors. We present an iterative shadowing compensation scheme that performs in a reconstruction-compensation loop manner using the shadowing compensation model, which is derived based on the angle distribution of backscattered electrons in two steps. In the first step, we deduce the model with some temporally assumptions for the convenience of modeling; In the second step, we modified the model by incorporating certain practical factors. Such proposed method can robustly and automatically provide both a reliable 3D surface and compensated shadowless images. The three main contributions of this study are as follows: (1) The shadowing compensation model, which provides an important method for esti-

Manuscript received November 20, 2012.
Manuscript revised April 19, 2013.

[†]The authors are with the Graduate School of Information Science and Technology, Hokkaido University, Sapporo-shi, 060–0814 Japan.
[††]The author is with the Yokohama Research Laboratory, Hitachi, Ltd., Yokohama-shi, 244–0817 Japan.
a) E-mail: chen@ssc.ssi.ist.hokudai.ac.jp
b) E-mail: atsushi.miyamoto.ts@hitachi.com
c) E-mail: kaneko@ssi.ist.hokudai.ac.jp

DOI: 10.1587/transinf.E96.D.2224

mating the underlying shadowless image intensity from an observed image with a shadowing effect, is introduced. (2) The shadowing compensation model is modified by including some practical factors to make it more accurate and applicable. (3) The iterative shadowing compensation method is proposed for eliminating shadowing effects in images and reconstructing a 3D shape iteratively.

The remainder of this paper is organized as follows: Section 2 gives a brief introduction to the SEM photometric stereo method. Sections 3 and 4 present the shadowing compensation model. The iterative surface reconstruction method is introduced in Sect. 5. Section 6 describes the experimental results, and Sect. 7 summarizes the main points of the research and suggests future studies.

2. Conceptualization of the Proposed SEM Photometric Stereo Method

The SEM photometric stereo method is substantially related to the photometric techniques used with an optical camera as measuring device [15]–[17] in that both are used to estimate gradient information for an object being observed from shading cues in the image data (The special case, in which the data is a single image, is generally known as shape from shading [18]–[20]). However, because of different imaging principles, the gradient estimation formulas are derived in different ways.

2.1 Basics

As schematically illustrated in Fig. 1 [7], in our SEM measurement system, two BSE detectors are symmetrically positioned along a direction. It is convenient for us to define this direction as an x-axis. Such a system can simultaneously provide two BSE images from the two detectors, denoted as BL and BR, respectively. In general, we use BL and BR to refer to the left and right image and detector 1 and 2 to designate the left and right detector, respectively. Suganuma [7] proposed an experimentally derived equation that could measure the gradient component in the direction of the x-axis (i.e., the slope $\tan\alpha$):

$$\frac{\partial z}{\partial x} = k\frac{BL^2 - BR^2}{(BL_n + BR_n)^2}, \tag{1}$$

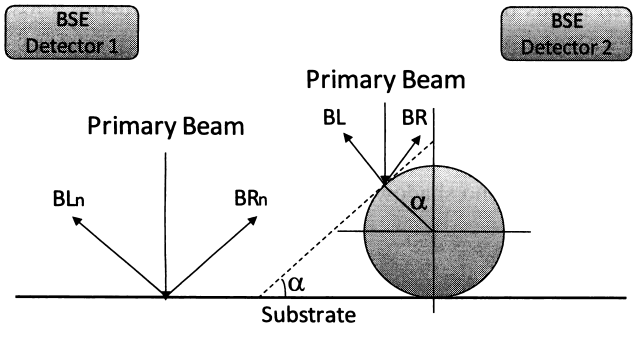

Fig. 1 Schematic diagram of measuring system with two BSE detectors.

where k is a constant and BL_n and BR_n are signal outputs from two detectors on the horizontal specimen surface.

2.2 Introducing a Shadowing Compensation Model

Suganuma's fitting model (1) can be effective provided the image intensities of both BL and BR are accurate. However, the gradient measurements are unreliable when applying in a region with shadowing effects. For dealing with shadowing errors, we improve the photometric stereo method by applying the following general ideas.

- **Shadowing Compensation Model**
  For eliminating shadowing errors, it is necessary to model the mechanism of generation of shadowing effects. To this end, we considered the angle distribution of backscattered electrons (BSEs) as a modified Lambert's cosine law. Using the angle distribution of BSEs, we explore how the BSE intensity (signal output) with shadowing errors is related to the underlying BSE intensity without shadowing errors. As a result, a shadowing compensation model is introduced, that can derive shadowless BSE intensities from shadowed measurements provided that the corresponding shadowing angles are known.
- **Improving the Shadowing Compensation Model**
  The shadowing compensation model is further modified by updating the BSE detection model. Three practical factors in the BSE detection process are in turn considered and further modeled by incorporating the corresponding three parameters, with which the accuracy and flexibility of the shadowing compensation model can be improved.
- **Estimating the 3D Surface and Shadowless Images**
  With a true 3D surface, we can calculate the shadowing angles and derive the underlying shadowless images from the original measured shadowed images using the shadowing compensation model. On the other hand, if shadowless images are provided, gradient measurements derived via Suganuma's equation could be accurate enough to estimate a reliable 3D surface. However, both these situations are the targets we are striving toward, and the problem essentially boils down to something such as a "chicken-and-egg" dilemma. We propose an iterative solution to the problem, that operates commutatively between shadowing compensation of the BSE images using the shadowing compensation model and reconstruction of the 3D surface from the compensated BSE images based on Suganuma's equation for calculating the gradient and a proposed noise-robust regularization optimization method for estimating depth from the gradient. After convergence of the iterative process, both a reliable 3D surface and shadowless images are provided.

The details regarding implementation of the preceding general ideas are presented in turn in the subsequent sections.

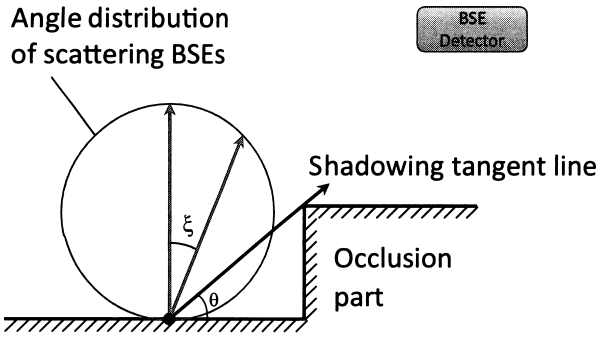

Fig. 2 Shadowing effect. BSEs emitted in a direction below the tangent line are generally absorbed by the occlusion region and consequently are not collected by the detector.

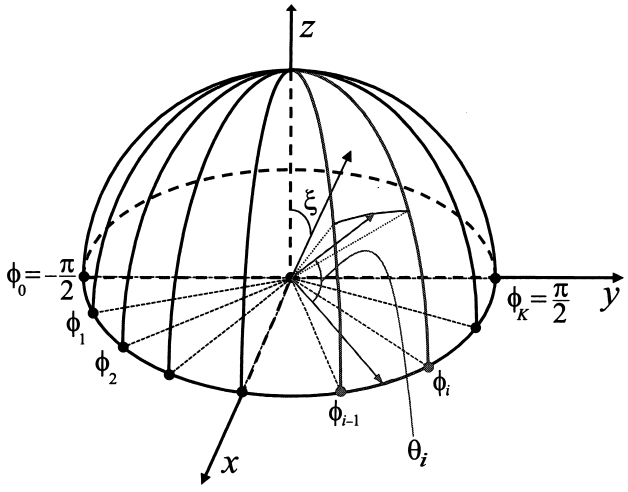

Fig. 3 Detectable region of a BSE detector.

3. Shadowing Compensation Model

Shadowing phenomena can frequently occur in imaging processes owing to the exceptional features of sample topography. As shown in Fig. 2, a portion of the electrons is screened out because of the occlusion, causing fewer electrons to be collected by the BSE detector. It is thus obvious that shadowing effects can contribute significantly to the final error of a reconstructed 3D surface if only model (1) is employed. Therefore, it would be advantageous if we could compensate the intensity observed under shadowing effects to obtain the underlying shadowless intensity by means of a compensation formula. We introduce such a shadowing compensation model under the following two assumptions:

1. The BSE image intensity is proportional to the amount of backscattered electrons (BSEs) collected by the detector.
2. The angle distribution of BSEs can be expressed as follows:

$$\frac{d\eta}{d\omega} = \frac{\eta_0}{\pi}(\cos\xi)^n, \tag{2}$$

where ξ describes the angle between the surface normal and the direction of the electron emission; η_0 is a coefficient; η and ω denote the quantity of BSEs and the solid angle, respectively; and the parameter n ensures more flexibility while describing the angular distribution in terms of the Lambert's cosine law, in which the parameter is equal to one [12].

In the following discussion, we restrict our problem domain to a situation in which the shadowing effect exists only in the horizontal region, in part, because the situation is generally common for measuring man-made structures such as semiconductors, whose height or shape need to be controlled precisely in manufacturing processes. In such restricted situation, the shadowing compensation model can be derived in a closed form.

For convenience, we temporally assume the occlusion phenomena and detecting ability of the detectors are ideal, i.e., the BSEs below the shadowing tangent line are totally absorbed and all the unshadowed BSEs are collected by the corresponding detectors.

3.1 BSE Intensity in the Absence of Shadowing

Based on the ideal detecting ability assumption on the detectors, in the case of no shadowing, a BSE detector (the right detector for consideration) ideally collects BSEs in a quarter sphere region, Ω_Q: $-\frac{\pi}{2} \le \phi \le \frac{\pi}{2}, 0 \le \xi \le \frac{\pi}{2}$. Here ϕ and ξ denote the azimuth and zenith angles, respectively (see Fig. 3). It is convenient for us to just assume the intensity of a single BSE image (left or right) at a point of observation reflects the amount of BSEs collected by the corresponding detector. Therefore, the BSE intensity without shadowing can be derived as follows:

$$\begin{aligned} \mathrm{BSE}_{\mathrm{shadowless}} &= \int_{\Omega_Q} \frac{\eta_0}{\pi}(\cos\xi)^n \, d\omega \\ &= \frac{\eta_0}{\pi}\int_{-\pi/2}^{\pi/2} d\phi \int_0^{\pi/2} \cos^n\xi \sin\xi d\xi \\ &= \frac{\eta_0}{n+1}. \end{aligned} \tag{3}$$

3.2 BSE Intensity in the Presence of Shadowing

In the shadowing case, the BSE detectable region should be Ω_Q minus the occluded region. Without introducing a loss of generality, we assume that the right detector is shadowed (see Fig. 3). We denote such a detectable region under the shadowing condition as Ω_Q^S: $-\frac{\pi}{2} \le \phi \le \frac{\pi}{2}, 0 \le \xi \le \frac{\pi}{2} - \theta(\phi)$. Here, $\theta(\phi)$ is the shadowing angle along the ϕ direction, which generally varies for different values of ϕ. Similar to the case with no shadowing, the intensity can be derived by

$$\begin{aligned} \mathrm{BSE} &= \int_{\Omega_Q^S} \frac{\eta_0}{\pi}(\cos\xi)^n \, d\omega \\ &= \frac{\eta_0}{\pi}\int_{-\pi/2}^{\pi/2} d\phi \int_0^{\pi/2-\theta(\phi)} \cos^n\xi \sin\xi d\xi. \end{aligned} \tag{4}$$

A problem here, however, is that an analytical expression for $\theta(\phi)$ is unlikely to be accessible. This issue can be resolved by dividing the detectable region Ω_Q^S into small segment regions defined as Ω_i^S: $\phi_{i-1} \le \phi \le \phi_i$, $0 \le \xi \le \frac{\pi}{2} - \theta(\phi)$, $1 \le i \le K$. It is reasonable to assume that the shadowing angle within each small region Ω_i^S remains approximately constant, that is, $\theta(\phi) \approx \theta_i$ for $\phi_{i-1} \le \phi \le \phi_i$, $1 \le i \le K$. Hence, we can calculate the BSE intensity under these circumstances as follows:

$$\begin{aligned}\mathrm{BSE} &= \int_{\Omega_Q^S} \frac{\eta_0}{\pi} (\cos\xi)^n d\omega = \sum_{i=1}^{K} \int_{\Omega_i^S} \frac{\eta_0}{\pi} (\cos\xi)^n d\omega \\ &= \frac{\eta_0}{\pi} \sum_{i=1}^{K} \int_{\phi_{i-1}}^{\phi_i} d\phi \int_0^{\pi/2-\theta(\phi)} \cos^n\xi \sin\xi d\xi \\ &\approx \frac{\eta_0}{\pi} \sum_{i=1}^{K} \int_{\phi_{i-1}}^{\phi_i} d\phi \int_0^{\pi/2-\theta_i} \cos^n\xi \sin\xi d\xi \\ &= \frac{\eta_0}{n+1} \cdot \sum_{i=1}^{K} \frac{1-\sin^{n+1}\theta_i}{K}. \end{aligned} \tag{5}$$

In (5), it is obvious that the larger the segment K number, the greater the accuracy of the intensity value. Moreover, the derived intensity would achieve the actual value in the limiting case where $K \to +\infty$.

3.3 Shadowing Compensation Model

Equations (5) model the BSE intensity under the shadowing condition. In fact, the shadowless case can be considered as a special shadowing case in which all the shadowing angles are zero, which can be verified by setting $\theta_i = 0$ in Equations (5). Generalizing this observation, we can deduce the following shadowing compensation model by combining (3) and (5).

$$\mathrm{BSE}_{\mathrm{shadowless}} = \mathrm{BSE} \Big/ \left(\sum_{i=1}^{K} \frac{1-\sin^{n+1}\theta_i}{K} \right). \tag{6}$$

This model provides an important cue for estimating the underlying shadowless BSE intensity from an observed BSE intensity constrained by shadowing effects.

4. Improvements to the Shadowing Compensation Model

In the previous section, we have derived the shadowing compensation model under the ideal setting on occlusion and detection of BSEs. To optimize the process for modeling shadowing effects, however, some practical factors must be considered.

4.1 Practical Modeling of Parameters

4.1.1 The Parameter $\phi_{\min}$

When calculating the BSE intensity using (3) and (5), in both case it was assumed that the range of ϕ was from $-\frac{\pi}{2}$ to $\frac{\pi}{2}$. Nonetheless, BSEs in the region where ϕ is near $\pm\frac{\pi}{2}$ generally cannot be detected owing to the practical limitations of the detector. To circumvent this shortfall, we introduce the parameter $\phi_{\min}$. As shown in Fig. 4 (a), the range of the azimuth angle ϕ in a practical detectable region becomes $-\frac{\pi}{2} + \phi_{\min} \le \phi \le \frac{\pi}{2} - \phi_{\min}$. Since $\Delta\phi = \pi/K$ is chosen to be very small (for sufficient accuracy of (5)), we can simply approximate $\phi_{\min}$: $\phi_{\min} = S\Delta\phi$, where $S = \left[\frac{\phi_{\min}}{\Delta\phi}\right]$. Here, "[]" denotes the rounding operator. With such an approximation, the range of the azimuth angle ϕ in the practical detectable region is $\phi_S \le \phi \le \phi_{K-S}$. In particular, it is quite straightforward to derive new BSE intensity formulas from (3) and (5), which take the following forms:

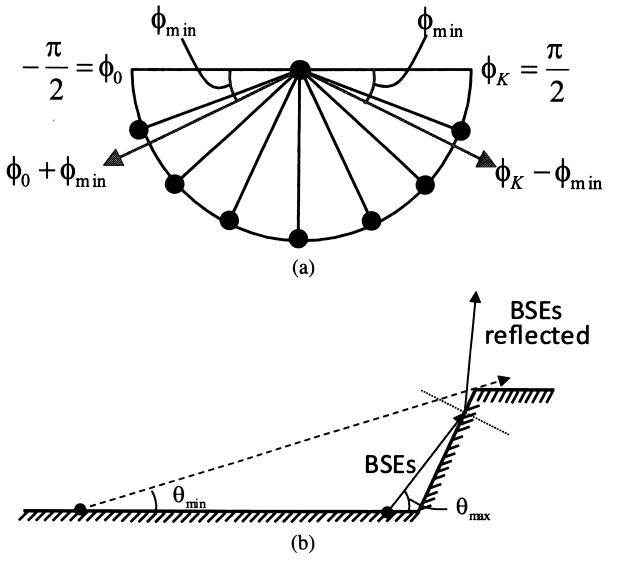

Fig. 4 Geometric representations of some practical factors: (a) $\phi_{\min}$ and (b) $\theta_{\min}$ and $\theta_{\max}$.

$$\mathrm{BSE}_{\mathrm{shadowless}} = \frac{K-2S}{K} \cdot \frac{\eta_0}{n+1}, \tag{7}$$

$$\mathrm{BSE} = \frac{K-2S}{K} \cdot \frac{\eta_0}{n+1} \cdot \sum_{i=S+1}^{K-S} \frac{1-\sin^{n+1}\theta_i}{K-2S}. \tag{8}$$

4.1.2 The Parameter $\theta_{\min}$

On account of the finite size of practical detectors, electrons with an emission direction near the horizontal plane may not be collected. For a point with a shadowing angle whose tangent line lies below the lowest detectable electron emission direction, there is no actual shadowing effect. Hence, in order to eliminate such false shadowing effects, one can simply establish a threshold, $\theta_{\min}$, such that shadowing angles that below the threshold are set to zero.

4.1.3 The Parameter $\theta_{\max}$

We previously gave the ideal assumption on occlusion phenomena, that the BSEs below the shadowing tangent line

were totally absorbed. However, as illustrated in Fig. 4 (b), when the emission direction of the BSEs is nearly parallel to the slope of the shadowing object (considerably large incident angle), the electrons are likely to be re-scattered rather than absorbed into the shadowing objects. Such reflected portion of BSEs is consequently detectable, which gives rise to increasing the corresponding image intensity and decreasing shadowing effects. While this phenomenon is generally difficult to model exactly due to the complicated dependence on the structure of the occlusion part, we thus approximately model it in a simple yet practically useful way by setting another threshold, $\theta_{\max}$, for the shadowing angle. When the shadowing angle is larger than $\theta_{\max}$, it is set to $\theta_{\max}$ to eliminate false shadowing effects resulted from unshadowed portion (reflected portion) of BSEs.

4.2 Modified Shadowing Compensation Model

Summarizing these practical factors, we ultimately obtain a modified shadowing compensation model that can be expressed as follows:

$$\mathrm{BSE}_{\mathrm{shadowless}} = \mathrm{BSE} / \left(\sum_{i=S+1}^{K-S} \frac{1 - \sin^{n+1} \theta_i}{K - 2S} \right), \tag{9}$$

with the thresholding operation

$$\theta_i = \begin{cases} 0 & \theta_i \le \theta_{\min}, \\ \theta_{\max} & \theta_i \ge \theta_{\max}, \\ \theta_i & \text{otherwise}, \end{cases}$$

for $S + 1 \le i \le K - S$.

In comparison with the primitive model (6), the modified one should be more accurate and flexible. Applying model (9) to a measured BSE image (*BL* or *BR*) at each point (pixel), we could estimate the underlying corresponding shadowless BSE image intensities from the measured ones, provided the shadowing angles for each point are known. Furthermore, there is no need to treat the points with shadowing errors separately from those without such errors, since the image intensity at a point without a shadowing effect (shadowing angles should be zero after implementation of the thresholding operator) remains the same after applying (9). Therefore, in contrast to a literature example [11], this case does not require an image segmentation process to extract shadowing regions, which is generally very difficult to implement.

5. Estimation of the 3D Surface and Shadowless Images

5.1 Depth from the Gradient

Suganuma's equation (1) measures the gradient component in the direction of the x-axis rather than measuring the height directly. Therefore it is necessary to calculate the depth from the gradient measurements. A discussion of this problem may appear to be out of place here, but it is included because previous SEM photometric stereo research studies have exploited this element to a very limited extent. For convenience, we introduce a short-hand notation, $p(x, y)$, as follows:

$$p(x, y) = k \frac{BL^2 - BR^2}{(BL_n + BR_n)^2}.$$

In almost all the previous SEM photometric stereo studies, an integration method was applied in which the depth $z(x, y)$ was obtained by integrating from each initial point (x_0, y) along the direction of the x-axis, that is

$$z(x, y) = z(x_0, y) + \int_{x_0}^{x} p(x, y) dx. \tag{10}$$

This integration method is very simple; however, it has a drawback in that it performs poorly when the data are noisy. A remedy is to reduce the level of noise, for instance, by averaging multiple images from the same static "scene" over time. However, it is generally expensive to obtain the large number of images required for this process.

An alternative is to allow a reconstruction algorithm to deal with the noise issue. To this end, we implement optimization techniques to find the best-fit surface z through minimization of the energy functional

$$\mathbf{E} = \iint_I \left[\frac{1}{2} \left(\frac{\partial z}{\partial x} - p(x, y) \right)^2 + \lambda \left| \frac{\partial z}{\partial y} \right| \right] dxdy \tag{11}$$

over some domain I (a rectangle region commonly) of the image. The first term, $\frac{1}{2} \left(\frac{\partial z}{\partial x} - p(x, y) \right)^2$, designated as the data term, functions to guarantee that the gradient component in the x direction of the reconstructed surface is as close to the measurement $p(x, y)$ as possible. The second term, called the smoothness term, operates to penalize the roughness in the y direction under the assumption that neighboring points generally have similar slopes in this direction. Here λ is a positive scalar factor that weights the relative contributions of these two terms, which can be set at a minimal value when the gradient measurement $p(x, y)$ is less noisy. This optimization method is also known as the regularization method [13], [14].

As the convexity of the functional (11) guarantees a unique global minimum, solving the functional minimization problem is equivalent to solving the corresponding Euler-Lagrange equation [21]:

$$(z_{xx} - p_x) + \lambda \frac{\partial}{\partial y} \left(\frac{z_y}{\sqrt{(z_y)^2 + \epsilon^2}} \right) = 0. \tag{12}$$

Here, ϵ is a small constant used to regularize the potential in cases where the denominator is zero (or approaches zero).

For numerical implementation, we must first discretize (12) using a finite difference operator according to our particular $x-y$ coordinate system [†] (see Fig. 5) rather than commonly used $x' - y'$ coordinate system, because Suganuma's

[†]In this case, the SEM used for our experiment performs raster scanning along the direction located 45° from the x-axis.

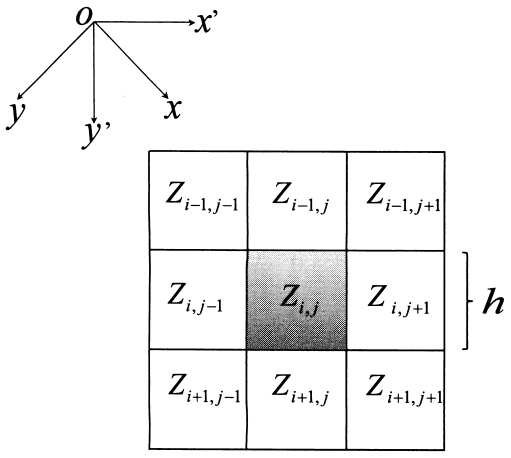

Fig. 5 Image coordinates.

equation measures the gradient component in the x direction with respect to the image plane:

$$\frac{z_{i+1,j+1} - 2z_{i,j} + z_{i-1,j-1}}{(\sqrt{2}h)^2} + \lambda\frac{\left(z_{i+1,j-1} - z_{i,j}\right)}{(\sqrt{2}h)^2 \cdot \Psi_1} + \lambda\frac{\left(z_{i-1,j+1} - z_{i,j}\right)}{(\sqrt{2}h)^2 \cdot \Psi_2} = \frac{p_{i+1,j+1} - p_{i-1,j-1}}{2(\sqrt{2}h)}, \tag{13}$$

where

$$\begin{cases} \Psi_1 = \sqrt{\left(\dfrac{z_{i+1,j-1} - z_{i,j}}{\sqrt{2}h}\right)^2 + \epsilon^2}, \\ \Psi_2 = \sqrt{\left(\dfrac{z_{i-1,j+1} - z_{i,j}}{\sqrt{2}h}\right)^2 + \epsilon^2}. \end{cases}$$

Moreover, boundary conditions need to be imposed to provide a unique solution. Here the commonly used Neumann boundary conditions are employed. The depth can be obtained by solving such a large but sparse nonlinear system. For instance, one efficient method is the nested fixed point iterative method [23].

5.2 Iterative Shadowing Compensation

As mentioned, gradient measurements derived via model (1) contain gross errors in the region with the shadowing effect. In contrast to the noise influence, such gross errors generally cannot be removed by model (11). A reasonable mechanism for dealing with the shadowing effect is to first eliminate shadowing effects in the images (*BL* and *BR*) by revising the observed image intensities using shadowing compensation model (9), which we have introduced previously, then applying models (1) and (11) in turn to obtain an accurate 3D shape. Unfortunately, a sufficiently accurate estimation of the underlying shadowless image intensity by means of (9) requires sufficiently accurate values for the corresponding shadowing angles. However, the true shadowing angles can only be calculated from the true 3D shape, which is, in fact, the target we are pursuing. As shadowing angles cannot be provided in advance, the shadowing compensation is conducted as an iterative procedure, as shown in Fig. 6.

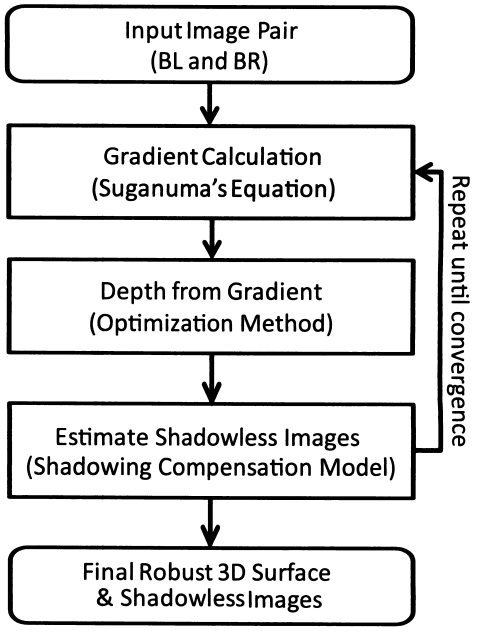

Fig. 6 Iterative scheme for surface reconstruction.

Iterative Surface Reconstruction Algorithm

1. Reconstruction of the 3D surface z^0 from the original images *BL* and *BR* by implementing (1) and (11) in turn.
2. At the k^{th} iteration, the shadowing angles are calculated first on the basis of the reconstructed surface z^{k-1} from the previous iteration. These shadowing angles are not the actual ones, but approximations. The image intensities in both *BL* and *BR* are then revised by applying shadowing compensation model (9). The compensated images are denoted as BL_c^k and BR_c^k.
3. Using models (1) and (11) again, a new approximation of the real surface z^k is reconstructed from BL_c^k and BR_c^k.
4. If the difference between z^k and z^{k-1} is smaller than the given threshold, the algorithm will be terminated; otherwise, the iteration will be repeated.

After convergence of the algorithm, both the reconstructed 3D surface and compensated shadowless images are obtained.

6. Experiments

In this section, we present the results of experiments on real image data and examine the robustness and effectiveness of the proposed method under shadowing conditions. The SEM used in our experiment has a general electron optics system except that the two BSE detectors are located 45° from the x'−axis (Fig. 5). Three different patterns with

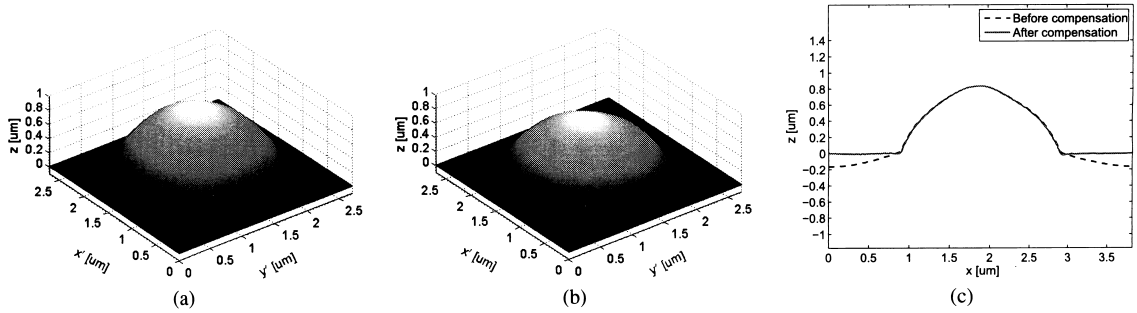

Fig. 8 Three-dimensional surfaces and section profiles of the "sphere" pattern before and after shadowing compensation: (a) 3D surface before compensation, (b) 3D surface after compensation, and (c) diagonal section profiles.

Table 1 Experimental parameters.

k	1.98
n	1.30
$\phi_{\min}$	16.9°
$\theta_{\min}$	17.5°
$\theta_{\max}$	55.0°

strong shadowing effects are used for evaluating the proposed reconstruction method, which include a standard particle with a "sphere" pattern, a semiconductor device with a "line" pattern, and a semiconductor device with a "concave" pattern having an embedded defect. The parameters used in the experiments are shown in Table 1. From a computational perspective, the calibration of parameters should be theoretically designed based on the information of corresponding physical processes, such as electron scattering characteristics, detectable ranges of detectors, signal conversion characteristics (conversion from the amount of detected BSEs to image intensity), etc. However, it is difficult to accurately know such information in practice. We therefore manually determine the parameters by observing that the reconstructed shape do not have distortions. As the experiments of the three patterns share the one set of parameters, we consider that it should not be overfitting for each individual case. However, in the field of SEM photometric stereo method, one set of universally utilized parameters might not be sufficient owing to the use of different materials, imaging conditions, and so on. Therefore, we recognize this as a problem for future investigation requiring some data-wise optimization of the parameters.

Figures 7 and 8 show experimental results for the "sphere" pattern. In this case, the sphere particle plays the role of the occlusion. As described in the previous section, the existence of a shadowing effect results in an image intensity that is smaller than the underlying shadowless one. As mentioned before, the detectors are set along the diagonal direction with respect to the image plane. Therefore, the shadowing effects of the sphere pattern occur mainly in the area of the diagonal, (i.e., the lower-right flat region in the left image and the upper-left flat region in the right image). As shown in Fig. 7 (a) and (b), the brightness in the shadowing regions is less intense than that in the flat regions without shadowing. Whereas, as shown in Fig. 7 (c) and (d),

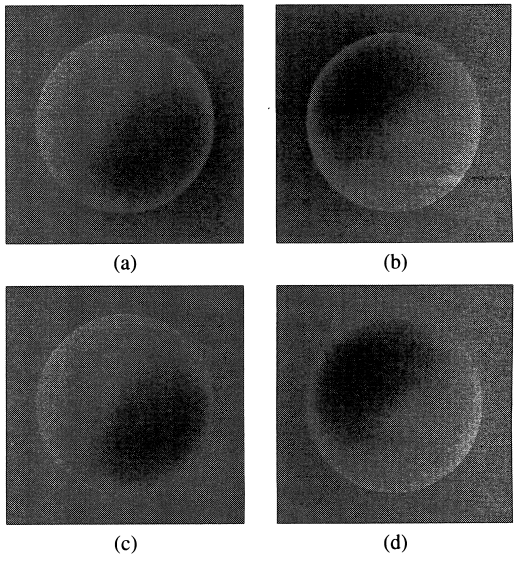

Fig. 7 Comparison between the original and compensated images of the "sphere" pattern: (a) original *BL* image, (b) original *BR* image, (c) compensated *BL* image, and (d) compensated *BR* image.

the brightness of the flat region around the spherical particle in both the left and right compensated image demonstrates a certain uniformity, which in turn implies good compensation of the image intensities. As shown in Fig. 8, shape distortion in the flat region resulting from shadowing errors, i.e., a rising-slope toward the sphere, can be effectively reduced by compensation.

Figures 9 and 10 show reconstruction results for the "line" pattern. The original left and right images (*BL* and *BR*) are shown in Fig. 9 (a) and (b). It is obvious that the right side of the left image and the left side of the right image are notably dark, which is, in fact, due to shadowing effects. In this case, the "line" plays the role of the occluding object. Such shadowing errors in image intensities give rise to significant departures of the gradient measurements from true ones (zeros at ideally flat regions), which is consequently reflected in the reconstructed 3D surface as a rising slope toward the "line" (see Fig. 10). As shown in Fig. 9 (c) and (d), these dark shadowing regions in the original left and right images are effectively eliminated in the

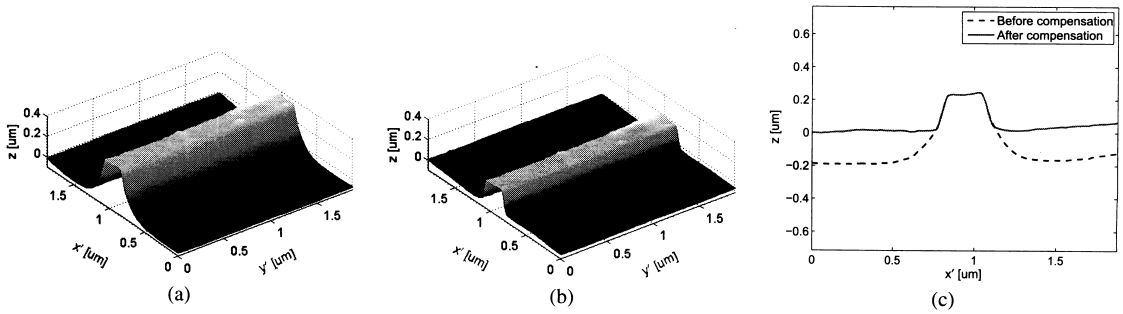

(a) (b) (c)

Fig. 10 Three-dimensional surfaces and section profiles of the "line" pattern before and after shadowing compensation: (a) 3D surface before compensation, (b) 3D surface after compensation, and (c) center horizontal section profiles.

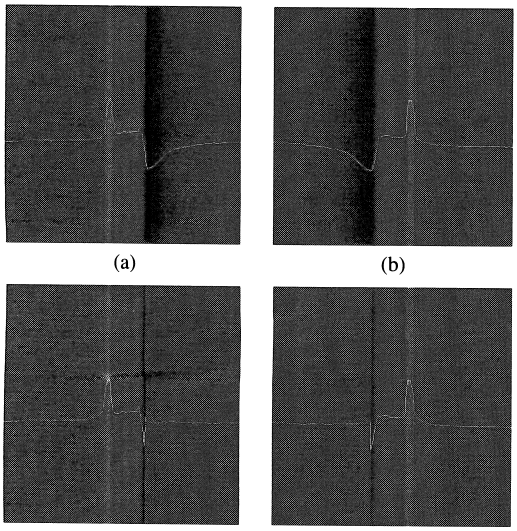

(a) (b) (c) (d)

Fig. 9 Comparison between the original and compensated images of the "line" pattern: (a) original *BL* image, (b) original *BR* image, (c) compensated *BL* image, and (d) compensated *BR* image. The plot of every image shows average column intensities.

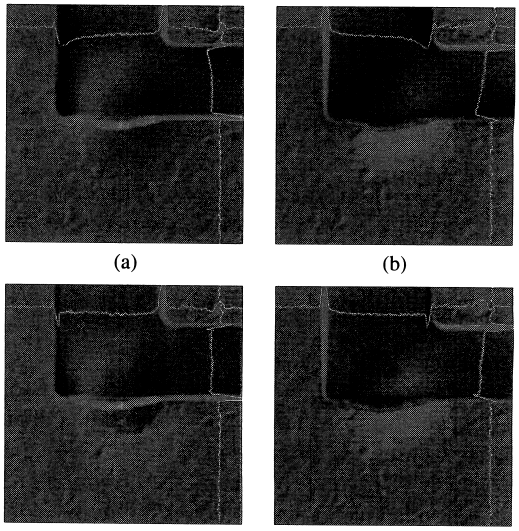

(a) (b) (c) (d)

Fig. 12 Comparison between the original and compensated images of the "concave" pattern: (a) original *BL* image, (b) original *BR* image, (c) compensated *BL* image, and (d) compensated *BR* image.

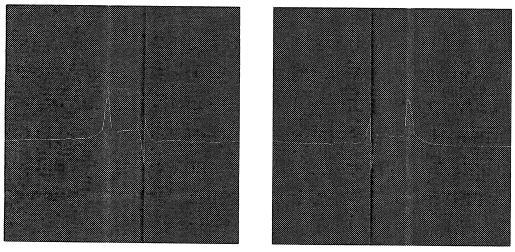

(a) (b)

Fig. 11 Over-compensated images of the "line" pattern: (a) over-compensated *BL* image and (b) over-compensated *BR* image.

compensated images. The corresponding average intensity plots (the average is used to avoid submersion of the plot into noise) also highlight suitably compensated shadowing errors. Moreover, the reconstructed 3D surface shape and section profile also show large modifications (Fig. 10) in that the rising slope regions on both sides of the "line" are properly corrected to a nearly flat level.

On account of the good illustrative property of the "line" pattern (the average intensity plot was easily drawn to demonstrate the shadowing and compensation conditions), we designed an additional experiment using the "line" pattern to demonstrate the significance of the parameter $\theta_{\max}$, which is introduced for improving the accuracy and flexibility of the shadowing compensation model (Section 4.1.3). To this end, the same computational process is implemented except that the value of $\theta_{\max}$ was set to $\frac{\pi}{2}$, which is equivalent to omitting the thresholding operation with $\theta_{\max}$. The resulting compensated shadowless image pair is shown in Fig. 11. Compared to the result in Fig. 9 (c) and (d), the average intensity plots show that shadowing regions very near to the "bar" are overcompensated resulting in much higher intensities, which indicates that the underlying true shadowing angels in that region should be smaller. The thresholding operation with $\theta_{\max}$ could generally overcome this problem well and consequently contribute greater accuracy to the shadowing compensation model.

Figures 12 and 13 show experimental results for the

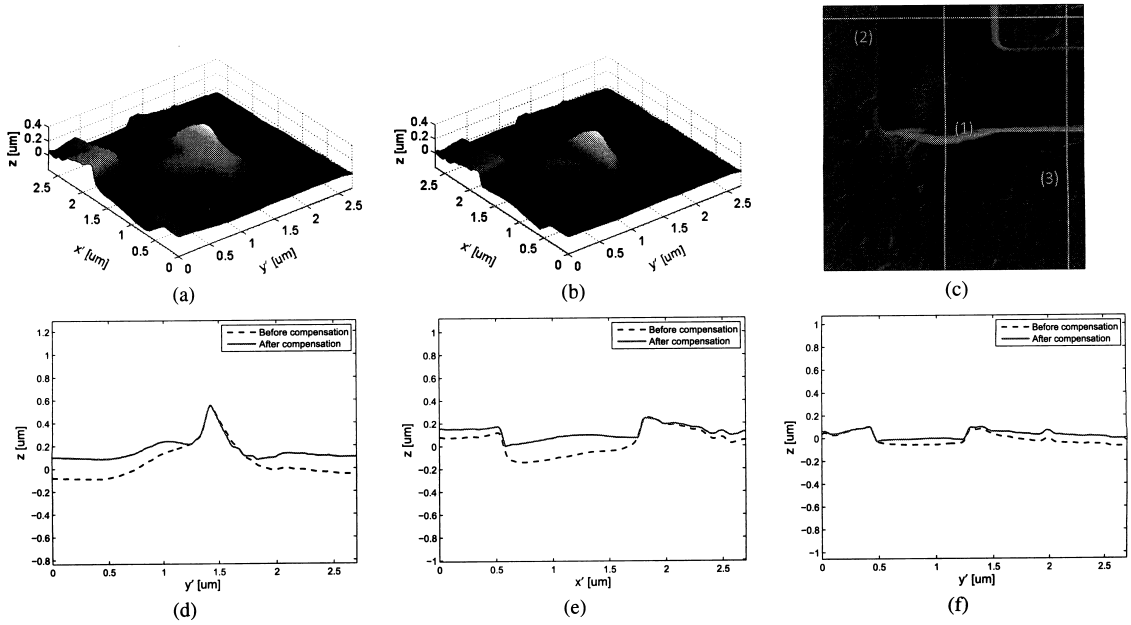

Fig. 13 Three-dimensional surface and section profiles of the "concave" pattern before and after shadowing compensation: (a) 3D surface before compensation, (b) 3D surface after compensation, (c) selected section profile positions marked on the left image *BL*, (d) vertical section profiles crossing the defect at position (1), (e) horizontal section profiles at position (2), and (f) vertical section profiles at position (3).

"concave" pattern with an embedded defect. The topography of the pattern is much more complicated than that of the previous two cases. As observed in the original left and right images in Fig. 12 (a) and (b), the image brightness near the sloping region is much lower, which is obviously due to the corresponding shadowing effect. This feature is also demonstrated more clearly by the average intensity plots (near positions (2) and (3) in Fig. 13 (c)). The shadowing effect on both sides of the defect "peak" is also strong, and although it is not readily distinguishable by the image brightness, it can be clearly observed in the 3D shape. The compensated shadowless images are shown in Fig. 12 (c) and (d). As seen in the figure, the regions that were dark in the original left and right images now show an appropriate level of brightness. The modification is highlighted by the corresponding average intensity plots, although they are not perfectly flat. Figure 13 (a) and (b) show the reconstructed 3D shape before and after shadowing compensation, respectively. As the "concave" pattern is substantially complicated to give a vivid view of the 3D surface modification afforded by the shadowing compensation process, we selected three representative section profiles, whose positions are marked in Fig. 13 (c). The first one is a vertical section crossing the "peak" shown in Fig. 13 (d). Because the "peak" is high, the shadowing effect on both sides is strong, which has a certain similarity to the "line" pattern where the "peak" plays the role of the "bar". Such shadowing errors result in a rising slope effect, as shown by the dashed line profile (before compensation), and this effect is reduced by shadowing compensation, as shown by the solid line. The other two section profiles, shown in Fig. 13 (e) and (f), have a similar shadowing effect. The shadowing error in the "concave" region results in a falling slope effect, leading to a deeper cavity, as shown by the dashed lines. After the shadowing compensation process, such falling slope effects are eliminated to a certain degree, as shown by the solid lines.

Table 2 Quantitative comparison (mean absolute error in horizontal regions).

	Before compensation	After compensation
Sphere	$0.0862\mu m$	$0.0307\mu m$
Line	$0.0412\mu m$	$0.0229\mu m$

In older to quantitatively assess the de-shadowing performance of our method, we choose the "sphere" and "line" patterns on account of their good illustrative property. As the shadowing effects only exist on the background areas, the reconstruction of the sphere part and line part (no shadowing) is not affected. We thus only need to focus on the background parts. The background regions can be effectively segmented out manually from left and right images. Based on the assumption that the background parts are even, the true height can be set to zero. In order to eliminate translation of the reconstructed height z (the shape of $z+c$ should be identical to that of z, where c is a constant), the reconstructed surfaces are registrated at the origin point, i.e., to translate the surfaces z vertically to (0,0,0). We use the mean absolute error of measured height (list in Table 2) in background parts to evaluate the reconstruction performance. The proposed method shows much smaller deviation compared to the traditional method with no shadowing compensation.

7. Conclusion and Future Work

In this paper, we have proposed a robust 3D surface reconstruction method in SEM. The shadowing effect, a frequent occurrence in SEM imaging processes, can be effectively eliminated by the iterative scheme associated with the shadowing compensation model. The reconstructed 3D surface in this paper can be robustly and automatically obtained under an existing shadowing condition. Furthermore, the resulting left and right compensated images provide a potential opportunity for improving the imaging performance of SEM devices. The proposed method has also been verified by our experimental results, which show its robustness and effectiveness.

Future studies designed to validate the feasibility of this approach in real applications are under consideration. For example, the proposed method should be evaluated on various semiconductor patterns in actual production lines with different processes and layouts. Moreover, we aim to utilize volume data from the estimated 3D surface as features for Automatic defect classification (ADC) [1], [22], which may diversify the classification categories and improve the accuracy of the classification process. As yield prediction and specification of process issues in a production line are still very difficult, the proposed technology is expected to enhance quick and highly precise process control capabilities via synthetic analysis of a combination of information, in addition to ADC, including defect distribution, defect composition, equipment history, etc.

References

[1] A. Miyamoto and T. Honda, "Development of surface/embedded particle classification algorithm for SEM-ADC," IEICE Trans. Inf. & Syst. (Japanese Edition), vol.J91-D, no.6, pp.1604–1612, June 2008.

[2] T. Oshima, S. Kimoto, and T. Suganuma, "Stereomicrography with a scanning electron microscope," Photogrammetric Engineering, vol.36, pp.874–879, 1970.

[3] G. Koenig, W. Nickel, J. Storl, D. Meyer, and J. Stange, "Digital stereophotogrammetry for processing SEM data," Scanning, vol.9, pp.185–193, 1987.

[4] O.V. Kholodilov, A.Y. Grigoryev, and N.K. Myshkin, "Reconstruction of true topographies of solid surfaces in scanning electron microscopes using secondary electrons," Scanning, vol.9, pp.156–161, 1987.

[5] J. Lebiedzik, "An automatic topographical surface reconstruction in the SEM," Scanning, vol.2, pp.230–237, 1979.

[6] I.C. Carlsen, "Reconstruction of true surface-topographies in scanning electron microscopes using backscattered electrons," Scanning, vol.7, pp.169–177, 1985.

[7] T. Suganuma, "Measurement of surface topography using SEM with two secondary electron detectors," J. Electron Microscopy, vol.34, no.4, pp.328–337, 1985.

[8] L. Reimer, R. Böngerler, and V. Desai, "Shape from shading using multiple detector signals in scanning electron microscopy," Scanning Microscopy, vol.1, no.3, pp.963–973, 1987.

[9] T. Czepkowski and W. Slówko, "Some limitations of surface profile reconstruction in scanning electron microscopy," Scanning, vol.18, pp.433–446, 1996.

[10] J. Paluszyński and W. Slówko, "Surface reconstruction with the photometric method in SEM," Vacuum, vol.78, pp.533–537, 2005.

[11] J. Paluszyński and W. Slówko, "Compensation of the shadowing error in three-dimensional imaging with a multiple detector scanning electron microscope," Scanning, vol.224, pp.93–96, 2006.

[12] L. Reimer, Scanning Electron Microscopy: Physics of Image Formation and Microanalysis, 2nd ed., pp.146–152, Springer, 2008.

[13] K. Sakaue, A. Amano, and N. Yokoya, "Optimization approaches in computer vision and image processing," IEICE Trans. Inf. & Syst., vol.E82-D, no.3, pp.534–547, March 1999.

[14] T. Poggio, V. Torre, and C. Koch, "Computational Vision and Regularization Theory," Nature, vol.317, pp.314–319, 1985.

[15] R.J. Woodham, "Photometric method for determining surface orientation from multiple images," Optical Engineering, vol.19, no.1, pp.139–144, 1980.

[16] D. Forsythe and J. Ponce, Computer Vision: A Modern Approach, pp.80–86, Prentice Hall, 2001.

[17] S. Barsky and M. Petrou, "The 4-source photometric stereo technique for three-dimensional surfaces in the presence of highlights and shadows," IEEE Trans. Pattern Anal. Mach. Intell., vol.25, no.10, pp.1239–1252, 2003.

[18] K. Ikeuchi and B.K.P. Horn, "Numerical shape from shading and occluding boundaries," Artif. Intell., vol.17, pp.141–184, 1981.

[19] B.K.P. Horn and M.J. Brooks, "The variational approach to shape from shading," Computer Vision, Graphics and Image Processing, vol.33, pp.174–208, 1986.

[20] B.K.P. Horn, "Height and gradient from shading," International Journal of Computer Vision, vol.5, pp.37–75, 1990.

[21] I.N. Bronstein, K.A. Semendyayev, G. Musiol, and H. Muehlig, Handbook of Mathematics, Fifth ed., Springer, 2007. ISBN 978-3540721215.

[22] K. Watanabe, Y. Takagi, K. Obara, H. Okuda, R. Nakagaki, and T. Kurosaki, "Efficient killer-defect control using reliable high-throughput SEM-ADC," Proc. 12th Annual IEEE/SEMI Advanced Semiconductor Manufacturing Conference, pp.219–222, 2001.

[23] C.R. Vogel and M.E. Oman, "Iterative methods for total variation denoising," SIAM Journal on Scientific Computing, vol.17, pp.227–238, 1996.

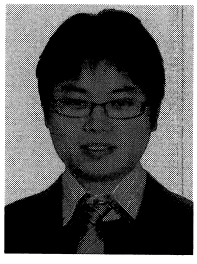

Deshan Chen received the M.S. degree in Information and Computing Science from Jilin University, China, in 2009. He is currently a Ph.D. student at Graduate School of Information Science and Technology, Hokkaido University, Japan. His research interests include computer vision and image processing.

Atsushi Miyamoto received the B.S. degree in precision engineering and the M.S. and Ph.D. degrees in system information engineering from Hokkaido University, Japan, in 1996, 1998, and 2001, respectively. He is currently a senior researcher at Yokohama Research Laboratory, Hitachi, Ltd., Japan. He received the Society Award in 1998 from Japan Society of Precision Engineering. His research interest includes robust image processing and statistical pattern recognition. He is a member of IEICE, JSPE, JAMIT, and IEEE.

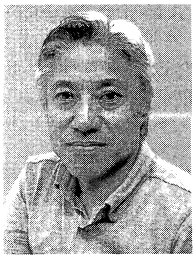

Shun'ichi Kaneko received the B.S. degree in precision engineering and the M.S. degree in information engineering from Hokkaido University, Japan, in 1978 and 1980, respectively, and then the Ph.D degree in systems engineering from the University of Tokyo, Japan, in 1990. He had been a research assistant of the Department of Computer Science since 1980 to 1991, an associate professor of the Department of Electronic Engineering since 1991 to 1995, and an associate professor of the Department of Bio-application and Systems Engineering since 1995 to 1996, in Tokyo University of Agriculture and Technology, Japan. He is a professor of the Laboratory of System Sensing and Control in the Graduate School of Information Science and Technology in Hokkaido University. He received the Best Paper Award in 1990, the Society Award in 1998, respectively, from Japan Society of Precision Engineering. His research interest includes machine vision, image sensing and understanding, robust image registration. He is a member of IEICE, JSPE, IEEJ, SICE and the IEEE computer society.